

Structural and magnetic phase diagram of CrAs and its relationship with pressure-induced superconductivity

Yao Shen^{‡,1} Qisi Wang^{‡,1} Yiqing Hao^{‡,1} Bingying Pan,¹ Yu Feng,¹ Q. Huang,² L. W. Harriger,² J. B. Leao,² Y. Zhao,^{2,3} R. M. Chisnell,² J. W. Lynn,² Huibo Cao,⁴ Jiangping Hu,^{5,6} and Jun Zhao^{*1,7}

¹ State Key Laboratory of Surface Physics and Department of Physics, Fudan University, Shanghai 200433, China

² NIST Center for Neutron Research, National Institute of Standards and Technology, Gaithersburg, Maryland 20899, USA

³ Department of Materials Science and Engineering, University of Maryland, College Park, Maryland 20742, USA

⁴ Neutron Scattering Science Division, Oak Ridge National Laboratory, Oak Ridge, Tennessee 37831-6393, USA

⁵ Institute of Physics, Chinese Academy of Sciences, Beijing 100190, China

⁶ Department of Physics, Purdue University, West Lafayette, Indiana 47907, USA

⁷ Collaborative Innovation Center of Advanced Microstructures, Nanjing 210093, China

Unconventional superconductivity in cuprates, iron-based superconductors, and heavy-fermions can be achieved through chemical doping or application of pressure on their magnetically ordered parent compounds [1–4]. The discovery of pressure-induced superconductivity in helimagnet CrAs therefore has generated great interest in understanding microscopic magnetic properties and their relationship to superconductivity [5, 6]. Here, we report the structural and magnetic phase diagram of CrAs as a function of temperature and pressure. We show that CrAs exhibits a spin reorientation from the *ab* plane to *ac* plane, along with an abrupt drop of the magnetic propagation vector at a critical pressure ($P_c \approx 0.6$ GPa). This magnetic phase transition coincides with the emergence of bulk superconductivity, indicating a direct connection between magnetism and superconductivity. With further increasing pressure, the magnetic order completely disappears near the optimal T_c regime ($P \approx 0.94$ GPa). Moreover, the Cr magnetic moments between nearest neighbors tend to be aligned antiparallel with increasing pressure toward the optimal superconductivity regime, suggesting that antiferromagnetic fluctuations are crucial to superconductivity.

CrAs has a MnP-type orthorhombic crystal structure at room temperature, which can be considered as a distorted hexagonal NiAs-type structure [8–12]. Previous measurements have shown that the system exhibits a first order helimagnetic phase transition accompanied by a magnetostriction below $T_N \approx 270$ K [8–12]. The resistivity of CrAs also exhibits a clear anomaly around the Néel temperature [5–7]. This anomaly is suppressed progressively under pressure and fades away at $P > 0.6$ GPa, before the bulk superconductivity appears [5, 6]. The maximum $T_c \approx 2$ K is attained at $P \approx 1$ GPa, above which the T_c decreases with increasing pressure [5, 6]. It has also been shown that the nuclear spin-lattice relaxation rate in CrAs shows substantial magnetic fluctuations, but does not display a coherence peak in the superconducting state, indicating an unconventional pairing mechanism [13]. Although these results suggest that CrAs is a pressure-induced unconventional superconductor, it remains unclear how the lattice and magnetic structures evolve under pressure as the system is tuned from a metallic helimagnet to a superconductor.

We used neutron scattering to study the structural and magnetic phase transitions of CrAs. Fig. 1c illustrates the diffraction pattern at 5 K at ambient pressure, which can be described by the orthorhombic *Pnma* space group together with a double helimagnetic structure (Fig. 1a). Similar to earlier work [9], the Cr magnetic moment [1.73(1) μ_B] lies in the *ab* plane, and the helical propagation vector is $\vec{k} = (0, 0, 0.3564)$ along the *c* axis at $T = 4$ K. Our magnetic refinements also suggest that the phase angle between the helices running through S_1 and S_2 is $\phi = -108.8(5)^\circ$, and that the angle between S_2 and S_3 is $\beta = 172.9(5)^\circ$ (Fig. 1a). We note that the phase angle ϕ is different from the values reported previously, which failed to describe our data.

To determine the evolution of the magnetic structure as a function of pressure, we carried out neutron powder diffraction measurements in an aluminium alloy or steel pressure cell. Fig. 1d shows the diffraction pattern in the aluminium alloy pressure cell at $P = 0.4$ GPa at $T = 4$ K. Magnetic refinements suggest that the magnetic structure is similar to that at ambient pressure, except for the slightly reduced propagation vector $(0, 0, 0.317)$ and moment [1.71(2) μ_B]. The most striking discovery is that the diffraction pattern

at $P = 0.6$ GPa (Fig. 1e) shows substantial changes of the magnetic reflections compared with those at ambient and low pressures, indicative of a magnetic phase transition. Our refinement analysis reveals that these changes are due to a spin reorientation from the ab plane to ac plane together with a rapid decrease of magnetic propagation vector to $\vec{k} = (0, 0, 0.2079)$, as shown in Fig. 1b. The strongly pressure dependent propagation vector and spin rotation plane implies that the helimagnetic order mainly arises from the exchange coupling between local moments. Indeed, the decrease of the magnetic propagation vector can be qualitatively understood by considering a minimum magnetic exchange model based on the nearest neighbor spins and the Dzyaloshinskii-Moriya interactions. There are four spins in one unit cell, as labeled in Figs. 1a and 1b. The interaction between spin \hat{S}_i and \hat{S}_j can be generally written as:

$$\hat{H}_{ij} = \vec{D}_{ij} \cdot (\hat{S}_i \times \hat{S}_j) + J_{ij} \hat{S}_i \cdot \hat{S}_j, \quad (1)$$

where the first term is the Dzyaloshinskii-Moriya interaction. As the component of \vec{D} along the c axis is larger than the one along the b axis, the propagation vector decreases when the helix rotation plane changes from the ab plane to ac plane (detailed calculations are described in the Supplementary Information). In addition, the crystallographic structure refinements suggest that the nuclear peaks can be described by an orthorhombic $Pnma$ space group for all pressures and temperatures measured. The refined atomic positions at representative temperature and pressure are given in Table I.

Figure 2 summarizes the structural and magnetic phase transitions under various pressures. At ambient pressure, $(0, 0, 0) \pm$ magnetic peak abruptly disappears on warming to $T_N = 272$ K, suggesting a first order magnetic phase transition (Figs. 2a and 2k). Similar behavior is also observed at $P = 0.4$ GPa (Figs. 2c and 2l). At the critical pressure $P_c = 0.6$ GPa, the magnetic peak shows a spin reorientation behavior from the ab plane to ac plane below $T_r = 88$ K (Figs. 2e and 2m). With further increasing pressure to $P = 0.72, 0.82$ GPa, the magnetic moment stays in the ac plane, while its magnitude is further reduced. Accompanied by the magnetic phase transitions, structural phase transitions are also observed under various pressures (Figs. 2b, 2d, 2f, 2h, 2j, and 2k-2o), even though the crystal symmetry remains unchanged below and above the

Néel temperature. The temperature-dependent profile of nuclear peaks shows a sudden shift near the Néel temperature, indicative of discontinuous changes of lattice parameters (Figs. 2b, 2d, 2f, 2h, and 2j). The structural phase transition occurs at the same temperature as the onset of the magnetic order at all pressures measured (Figs. 2k-2o). Interestingly, we notice that the magnetic peak positions also shift progressively on cooling, indicating that the propagation vector is also temperature-dependent (Figs. 2a, 2c, 2e, 2g, and 2i). Fig. 3a summarizes the pressure and temperature dependence of the propagation vector. Obviously, the propagation vector decreases gradually with decreasing temperature at $P = 0$ and 0.4 GPa, where the magnetic moment is in the *ab* plane (Fig. 3a), which is similar to previous results at ambient pressure [9]. On the other hand, the propagation vector actually increases slightly with decreasing temperature at $P = 0.72, 0.82$ GPa, where the magnetic moment has rotated to the *ac* plane. At the critical pressure $P_c \approx 0.6$ GPa, the propagation vector decreases drastically on cooling to below $T_r = 88$ K, owing to the spin reorientation from the *ab* plane to *ac* plane (Fig. 3a). The dramatically temperature-dependent magnetic propagation vector observed here is different from the weakly temperature-dependent spin density wave vector of metallic chromium [14].

To summarize the data in Figs. 1, 2 and 3a, we plot in Fig. 3b the structural and magnetic phase diagram of CrAs under pressure along with the superconducting transition temperatures determined from susceptibility measurements [5]. Both the magnetic and structural phase transition temperature and the magnetic moment are gradually suppressed by pressure and eventually completely disappear at $P \approx 0.94$ GPa, where optimal superconductivity (T_c is maximal) is realized (Figs. 3b and 3c). In contrast to previous resistivity measurements that suggest that the magnetic order is completely suppressed at above $P > 0.6$ GPa [5, 6, 12], our neutron data show that the magnetic order and structural distortion persist at $P = 0.72, 0.82$, and 0.88 GPa, where the resistivity anomaly disappears (Fig. 3b). As the pressure dependence of the propagation vector at 4 K shows a sudden drop at above $P_c = 0.6$ GPa (Fig. 3d), which is accompanied by the spin reorientation, the diminishing resistivity anomaly is very likely due to the spin reorientation tran-

sition. Interestingly, an anomaly on the Néel temperature vs. pressure curve is also observed at $P = 0.72$ GPa (Fig. 3b), probably due to the competition between the high propagation vector phase and the low propagation vector phase near the spin reorientation transition. More importantly, as shown in Fig. 3b, the contour propagation vector map and the superconducting transition temperature plot reveal close connection between superconductivity and the low propagation vector phase. Comparison of the propagation vector with the superconducting volume fraction as a function of pressure further suggests that the emergence of the bulk superconductivity is directly associated with the spin reorientation and the subsequent decrease of the propagation vector (Fig. 3d). These results indicate strong coupling between magnetism and superconductivity in this system.

Figure 4 illustrates the pressure effect of the lattice constants, bond distances, and angles between Cr moments at various temperatures obtained from our refinement analysis. At ambient pressure, a large magnetostriction ($\Delta b/b=3.45\%$, $\Delta a/a=-0.29\%$, $\Delta c/c=-0.84\%$, $\Delta v/v=2.28\%$, $P = 0$ GPa) is observed below the Néel temperature (Figs. 4a-4c). The increased volume of the unit cell below T_N naturally suggests that the magnetic order could be suppressed by reducing magnetostriction under pressure. However, as shown in Figs. 4a-4c, the magnetostriction ($\Delta b/b=5.69\%$, $\Delta a/a=-0.88\%$, $\Delta c/c=-1.36\%$, $\Delta v/v=3.33\%$, $P = 0.6$ GPa) actually increases with increasing pressure. On the other hand, our detailed refinement analysis suggests that the pressure significantly reduces the nearest neighbor bond lengths of Cr atoms (Figs. 4e and 4f), which could make the d electrons of Cr more itinerant, and therefore reduce the magnetic moment. More interestingly, the pressure dependence of lattice parameters in the magnetically order state displays a clear anomaly at the critical pressure $P_c = 0.6$ GPa (Fig. 4d), which corresponds to the spin reorientation transition and the emergence of the bulk superconductivity (Figs. 3b and 3d). These observations indicate a strong coupling between electronic, magnetic and lattice degrees of freedom in this system. We also notice that the angle ϕ between Cr moments S_1 and S_2 decreases drastically from $\sim -100^\circ$ (almost perpendicular) to $\sim -160^\circ$ (almost antiparallel) with increasing pressure to $P > 0.6$ GPa (Fig. 4g). And

the angle β between S_2 and S_3 is close to 180° and barely changes with pressure (Fig. 4h). These results suggest that the moments between the nearest neighbors tend to be antiferromagnetically aligned in the bulk superconductivity regime.

In summary, we have determined the structural and magnetic phase diagram of CrAs, as the system is changed from a helimagnetic metal to a superconductor under pressure. We show that CrAs exhibits a spin reorientation from the ab plane to ac plane, together with a rapid decrease of the magnetic propagation vector from $(0, 0, 0.3564)$ at ambient pressure to $(0, 0, 0.144)$ at above the critical pressure ($P_c \approx 0.6$ GPa), where bulk superconductivity begins to emerge. Moreover, the pressure significantly reduces the nearest-neighbor bond lengths of Cr atoms, which could make the electrons more itinerant and therefore reduce the magnetic moment, resulting in a magnetic phase diagram very similar to those of many unconventional superconductors [1–4]. Furthermore, the nearest neighbor spins tend to be aligned antiparallel near the optimal superconductivity regime under pressure. Our findings suggest that the antiferromagnetic fluctuations associated with the low magnetic vector phase are important for superconductivity in this system.

Method

Our polycrystalline sample was synthesized as reported in *ref.* [12]. Consistent with previous measurements, the susceptibility of our sample displays a clear anomaly near 272 K, indicating a magnetic phase transition [5, 6]. Our neutron scattering measurements were carried out on the BT-1 powder diffractometer, SPINS cold triple-axis spectrometer, and BT-7 thermal triple axis spectrometer at the NIST Center for Neutron Research. The neutron wavelengths employed were 1.5389 or 2.0785 Å using the Ge(311) monochromator at BT-1, 4.0449 Å using PG (002) monochromator at SPINS, and 2.36 Å using PG (002) monochromator at BT-7. The neutron-diffraction data Rietveld refinements are based on the program FULLPROF [15]. For the pressure effect measurements, the polycrystalline sample was loaded into an aluminium alloy ($P_{max} = 0.65$ GPa) or steel pressure cell ($P_{max} = 1$ GPa), which was connected to an external piston-driven pressure intensifier via a heated capillary line, and pressurized using helium as a pressure medium. All

pressure changes were executed while maintaining the pressure vessels above the PxT line of helium. For the measurements below the PxT line of helium, hydrostatic conditions were maintained by employing a “BURP” process (a careful pressurization procedure in order to ensure pressure homogeneity within the pressure cells).

Note added: After we finished this paper, we became aware of a related preprint[16], in which neutron diffraction measurements were performed at $P \leq 0.65$ GPa using a clamp pressure cell, and the data are similar to ours at ambient and low pressures before the spin reorientation transition.

[#]These authors contributed equally to this work. *Corresponding author: zhaoj@fudan.edu.cn.

References

- [1] Lee, P. A., Nagaosa, N. & Wen, X.-G. Doping a mott insulator: physics of high-temperature superconductivity *Rev. Mod. Phys.* **78**, 17-85 (2006).
- [2] Johnston, D. The puzzle of high temperature superconductivity in layered iron pnictides and chalcogenides. *Advances in Physics* **59** 803 (2010).
- [3] Stewart, G. R. Heavy-fermion systems *Rev. Mod. Phys.* **56**, 755 (1984).
- [4] Norman, M. R. The challenge of unconventional superconductivity. *Science* **332**, 196-200 (2011).
- [5] Wu, W. et al., Superconductivity in the vicinity of antiferromagnetic order in CrAs. Preprint at <http://arxiv.org/abs/1406.6431> (2014).
- [6] Kotegawa, H., Nakahara, S., Tou H. & Sugawara H. Superconductivity of 2.2 K under pressure in helimagnet CrAs. *J. Phys. Soc. Jpn.* **83** 093702 (2014)
- [7] Wu, W. et al., Low temperature properties of pnictide CrAs single crystal *Science China* **53**, 1207-1211 (2010).
- [8] Boller, H. & Kallel, A. First order crystallographic and magnetic phase transition in CrAs. *Solid State Comm.* **9**, 1699-1706 (1971).
- [9] Selte, K., Kjekshus, A., Jamison, W. E., Andresen, A. F. & Engebretsen, J. E. Magnetic structure and properties of CrAs. *Acta Chem. Scand.* **25**, 1703-1714 (1971).
- [10] Watanabe, H., Kazama, N., Yamaguchi, Y. & Ohashi, M. Magnetic structure of CrAs and Mn-substituted CrAs. *J. Appl. Phys.* **40**, 1128-1129 (1969).
- [11] Kazama, N. & Watanabe, H. Magnetic properties of $\text{Cr}_{1-x}\text{Mn}_x\text{As}$ system. *J. Phys. Soc. Jpn.* **30**, 1319-1329 (1971).
- [12] Zavadskii, E. A. & Sibarova, I. A. Some features of phase transition in chromium arsenide at high pressures. *Sov. Phys. JETP* **51**, 542-547 (1980).

- [13] Kotegawa, H., Tou, H., Sugawara, H., & Harima H. Unconventional superconductivity in the vicinity of strong first-Order helimagnetic transition in CrAs: ^{75}As -nuclear quadrupole resonance study. Preprint at < <http://arxiv.org/abs/1408.3185v1> > (2014).
- [14] Fawcett, E. Spin-density-wave antiferromagnetism in chromium. *Rev. Mod. Phys.* **60**, 209-283 (1988).
- [15] Rodriguez-Carvajal, J. Recent advances in magnetic structure determination by neutron powder diffraction. *Physica B* **192**, 55 (1993)
- [16] Keller, L. et al., Pressure dependence of the magnetic order in CrAs: a neutron diffraction investigation. Preprint at <<http://arxiv.org/abs/1409.5706>> (2014).

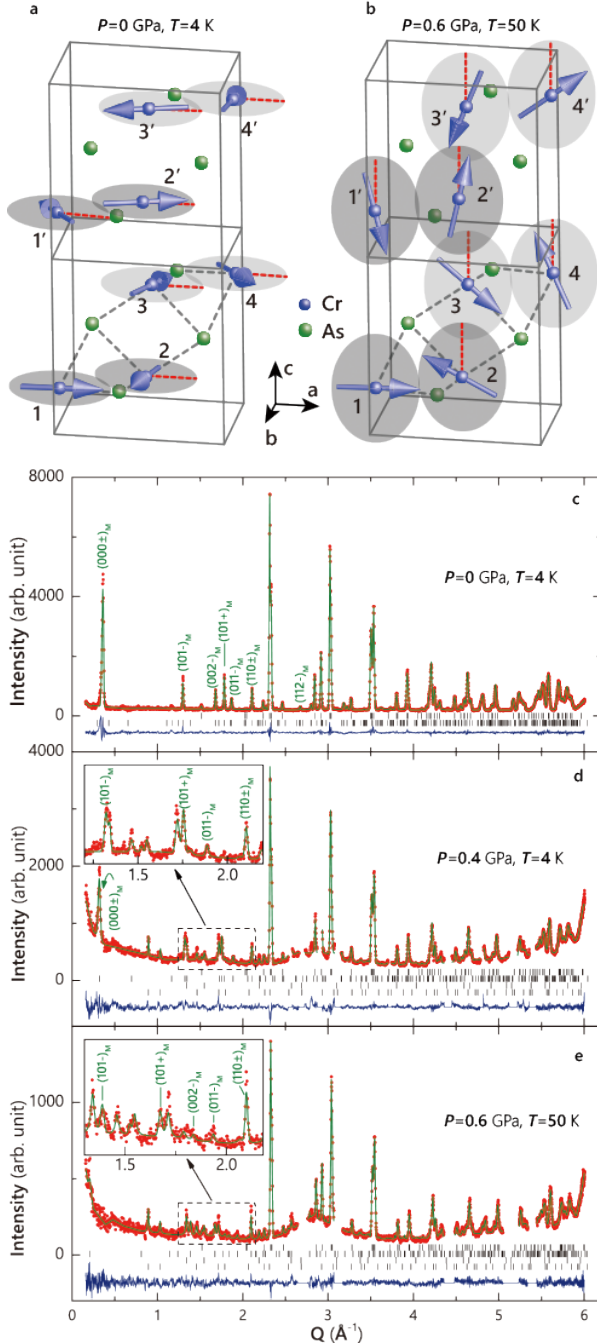


FIG. 1: **Pressure dependence of the magnetic structure for CrAs.** The neutron diffraction experiment was performed on the BT-1 diffractometer using a Ge (3,1,1) monochromator. The wavelength of the incident beam is $\lambda = 2.0785\text{\AA}$. **a**, Magnetic structure in CrAs at ambient pressure at $T = 4\text{ K}$ determined by our refinements. There are four Cr atoms in one unit cell. The magnetic moments on Cr lie in the *ab* plane. **b**, Magnetic structure in CrAs at $P = 0.6\text{ GPa}$ at $T = 50\text{ K}$. The Cr moment is in the *ac* plane. **c**, Observed (cross) and calculated (green) neutron powder diffraction intensities of CrAs at ambient pressure at 4 K. The spectrum is refined in the orthorhombic *Pnma* space group together with the magnetic structure shown in Fig. 1a. Short black vertical lines show the Bragg peak positions. The purple line indicates the difference between the observed and calculated intensities. Magnetic peaks are indexed in the figure. **d**, The diffraction spectrum measured in an aluminium alloy pressure cell at $P = 0.4\text{ GPa}$ at 4 K. Magnetic peaks are highlighted and indexed in the inset. The four refined phases are crystal and magnetic structure of CrAs, the second and third order neutron reflections from the aluminium pressure cell. The missing data correspond to the strong first order neutron reflections from the aluminium pressure cell. **e**, The diffraction spectrum measured at $P = 0.6\text{ GPa}$

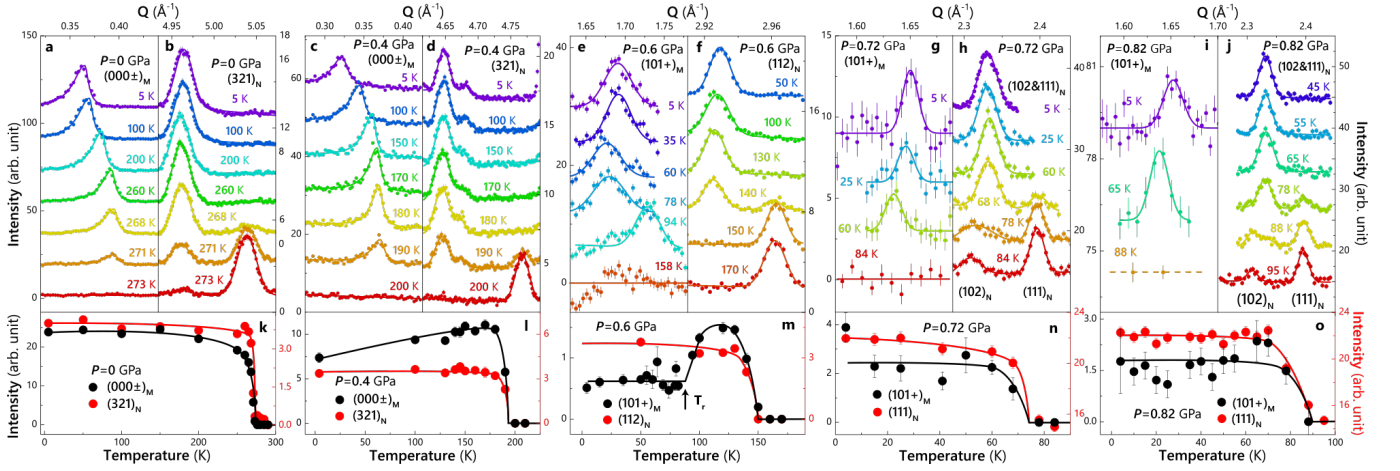


FIG. 2: **Structural and magnetic phase transition temperatures under various pressures in CrAs.** The data in **a-f** and **g-j** were collected in the aluminium alloy and steel pressure cell, respectively. **a-j**, Temperature-dependent diffraction profile of the magnetic and nuclear peaks at various pressures, (000 \pm) magnetic peak at $P = 0$ GPa, **a**; (321) nuclear peak at $P = 0$ GPa, **b**; (000 \pm) magnetic peak at $P = 0.4$ GPa, **c**; (321) nuclear peak at $P = 0.4$ GPa, **d**; (101+) magnetic peak at $P = 0.6$ GPa, **e**; (112) nuclear peak at $P = 0.6$ GPa, **f**; (101+) magnetic peak at $P = 0.72$ GPa, **g**; (102) and (111) nuclear peaks at $P = 0.72$ GPa, **h**; (101+) magnetic peak at $P = 0.82$ GPa, **i**; (102) and (111) nuclear peaks at $P = 0.82$ GPa, **j**. **k-o**, temperature dependence of the peak intensity of the data obtained in **a-j**. We note that in **l**, the decrease of the (000 \pm)_M peak intensity at low temperature is due to the decrease of the phase angle ϕ on cooling, as shown in Fig. 4g. The error bars indicate one standard deviation.

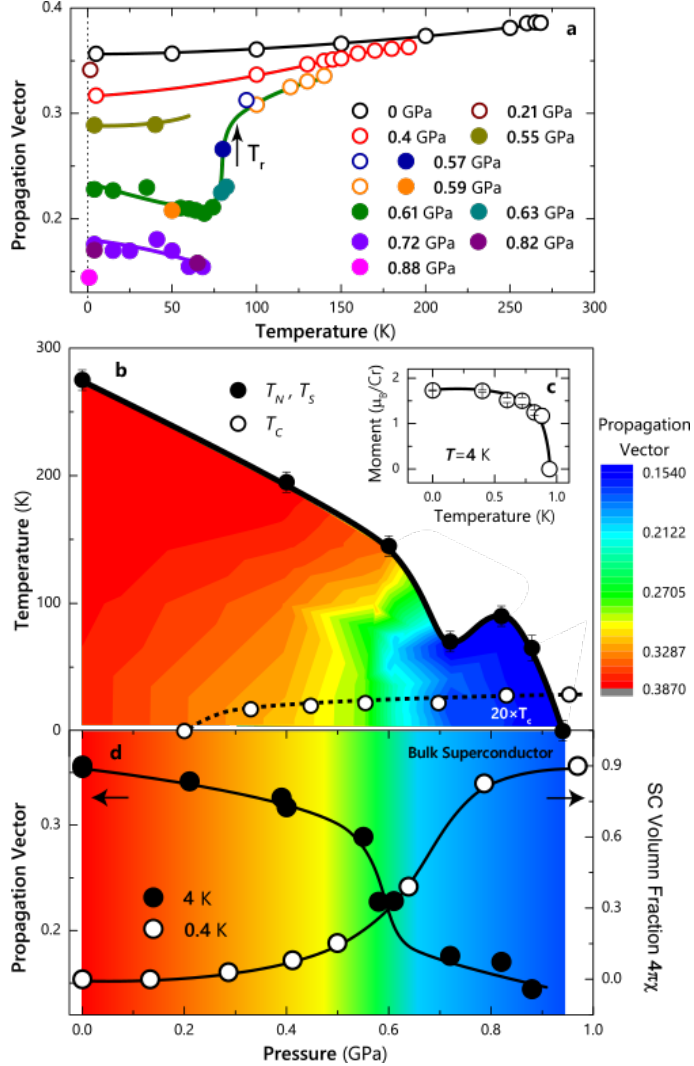


FIG. 3: Temperature and pressure dependence of the magnetic propagation vector and the structural and magnetic phase diagram of CrAs. **a**, Temperature and pressure dependence of the magnetic propagation vector. The open and filled circles indicate the magnetic moment in the *ab* and *ac* plane, respectively. **b**, Structural and magnetic phase diagram of CrAs. The contour propagation vector map is plotted with the data in Fig. 3a in the temperature-pressure space. The superconducting transition temperatures are adapted from *Ref.* [5]. **c**, The pressure dependence of the magnetic moment at 4 K. **d**, The pressure dependence of the propagation vector and the superconducting volume fraction determined by susceptibility measurements adapted from *Ref.* [5]. The error bars indicate one standard deviation.

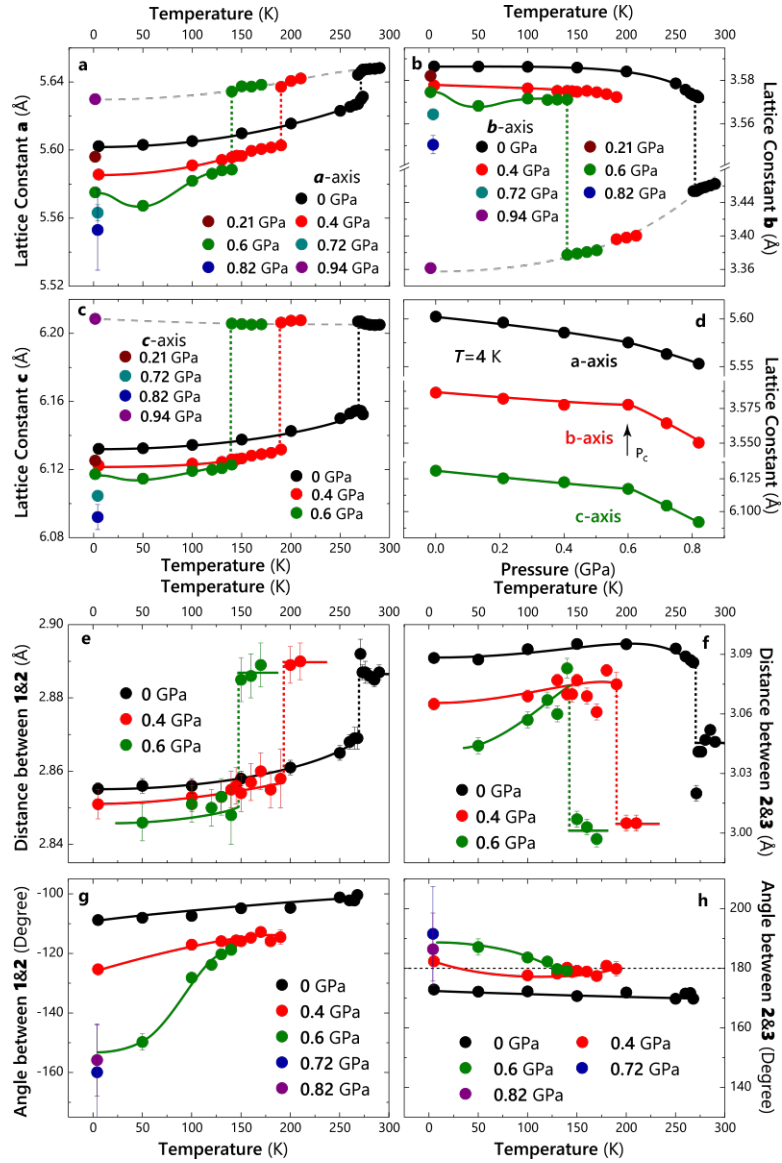


FIG. 4: Temperature and pressure dependence of lattice constants, bond distances, and angles between Cr moments obtained from the refinement analysis. **a-c**, Lattice parameter as a function of temperature and pressure. **d**, Pressure dependence of lattice parameter in the magnetically ordered state. A clear anomaly is observed near the critical pressure $P_c = 0.6$ GPa. **e**, Bond distance between S_1 and S_2 (nearest-neighbor). **f**, Bond distance between S_2 and S_3 (nearest-neighbor). **g**, Angle (ϕ) between spin S_1 and S_2 . **h**, Angle (β) between spin S_2 and S_3 . The error bars indicate one standard deviation.

TABLE I: Refined structural parameters of CrAs under various pressures. Space group: Pnma. Atomic positions: Cr: 4c (x, 1/4, z); As: 4c(x, 1/4, z).

<i>P</i>	<i>T</i>	<i>a</i>	<i>b</i>	<i>c</i>	<i>Cr</i> - <i>x</i>	<i>Cr</i> - <i>z</i>	<i>Cr</i> - <i>B</i>	<i>As</i> - <i>x</i>	<i>As</i> - <i>z</i>	<i>As</i> - <i>B</i>	<i>Rp</i>	<i>wRp</i>	χ^2
<i>GPa</i>	<i>K</i>	Å	Å	Å	Å ²						Å ²	%	%
0	4	5.60499(5)	3.58827(3)	6.13518(5)	0.0070(2)	0.2049(2)	0.15(2)	0.2045(1)	0.5836(1)	0.02(1)	4.83	5.87	1.55
0	290	5.65101(8)	3.46398(5)	6.20804(8)	0.0060(3)	0.2019(3)	0.74(5)	0.2016(2)	0.5766(2)	0.58(3)	6.03	7.84	1.52
0.4	4	5.5882(1)	3.57936(7)	6.1253(1)	0.0093(5)	0.2029(4)	0.14(5)	0.2026(2)	0.5837(3)	0.44(3)	4.73	5.95	2.00
0.4	210	5.6448(1)	3.40203(8)	6.2106(1)	0.0091(5)	0.1994(5)	0.32(6)	0.1985(3)	0.5738(3)	0.24(2)	4.49	5.77	1.27
0.6	50	5.5700(1)	3.57004(9)	6.1176(1)	0.0086(7)	0.2015(5)	0.08(8)	0.1990(3)	0.5822(4)	0.37(6)	5.84	7.03	1.11
0.6	170	5.64113(2)	3.38452(8)	6.20824(1)	0.0081(7)	0.1992(6)	0.27(8)	0.1979(4)	0.5726(4)	0.17(7)	5.40	6.69	0.972

Acknowledgements

Work at Fudan University is supported by the National Natural Science Foundation of China (Grant No. 11374059) and the Shanghai Pujiang Scholar Program (Grant No.13PJ1401100). H.C. received support from the Scientific User Facilities Division, Office of Basic Energy Sciences, US Department of Energy.